IVYSPRING INTERNATIONAL PUBLISHER

Theranostics

2016; 6(5): 739-751. doi: 10.7150/thno.14064

Research Paper

Designing 3D Mesenchymal Stem Cell Sheets Merging Magnetic and Fluorescent Features: When Cell Sheet Technology Meets Image-Guided Cell Therapy

Gabriel Rahmi[1,2]✉, Laetitia Pidial[1], Amanda K. A. Silva[3], Eléonore Blondiaux[1], Bertrand Meresse[4], Florence Gazeau[3], Gwennhael Autret[1], Daniel Balvay[1], Charles André Cuenod[1,5], Silvana Perretta[6], Bertrand Tavitian[1], Claire Wilhelm[3], Christophe Cellier[2], Olivier Clément[1,5]

1. Laboratoire Imagerie de l'Angiogénèse, Plateforme d'Imagerie du Petit Animal, INSERM U970, Université Paris Descartes, 56 Rue Leblanc, 75015 Paris, France.
2. Gastroenterology and Endoscopy Department, Hôpital Européen Georges Pompidou, APHP, Université Paris Descartes, 20 rue Leblanc, 75015 Paris, France.
3. Laboratoire Matières et Systèmes Complexes (MSC), UMR 7057 CNRS, Université Paris-Diderot, 10 rue Alice Domon et Léonie Duquet, 75205 Paris cedex 13, France.
4. Laboratory of Intestinal Immunity, Institut IMAGINE-INSERM 1163, 24 boulevard du Montparnasse, 75015 Paris, France.
5. Radiology Department, Hôpital Européen Georges Pompidou, APHP, Université Paris Descartes, 20 rue Leblanc, 75015 Paris, France.
6. Department of Digestive and Endocrine Surgery, Nouvel Hôpital Civil, and Institut de Recherche contre les Cancers de l'Appareil Digestif (IRCAD), 1 place de l'Hôpital, 67091 Strasbourg Cedex, France.

✉ Corresponding author: Gabriel Rahmi, M.D. gabriel.rahmi@egp.aphp.fr Laboratoire Imagerie de l'Angiogénèse, INSERM U970, Paris Descartes University. 56 Rue Leblanc, 75015, Paris, France. Tel: +33 6 23 25 01 55 Fax: +33 1 56 09 34 56

Received: 2015.10.07; Accepted: 2016.02.08; Published: 2016.03.21

Abstract

Cell sheet technology opens new perspectives in tissue regeneration therapy by providing readily implantable, scaffold-free 3D tissue constructs. Many studies have focused on the therapeutic effects of cell sheet implantation while relatively little attention has concerned the fate of the implanted cells *in vivo*. The aim of the present study was to track longitudinally the cells implanted in the cell sheets *in vivo* in target tissues. To this end we (i) endowed bone marrow–derived mesenchymal stem cells (BMMSCs) with imaging properties by double labeling with fluorescent and magnetic tracers, (ii) applied BMMSC cell sheets to a digestive fistula model in mice, (iii) tracked the BMMSC fate *in vivo* by MRI and probe-based confocal laser endomicroscopy (pCLE), and (iv) quantified healing of the fistula. We show that image-guided longitudinal follow-up can document both the fate of the cell sheet-derived BMMSCs and their healing capacity. Moreover, our theranostic approach informs on the mechanism of action, either directly by integration of cell sheet-derived BMMSCs into the host tissue or indirectly through the release of signaling molecules in the host tissue. Multimodal imaging and clinical evaluation converged to attest that cell sheet grafting resulted in minimal clinical inflammation, improved fistula healing, reduced tissue fibrosis and enhanced microvasculature density. At the molecular level, cell sheet transplantation induced an increase in the expression of anti-inflammatory cytokines (TGF-ß2 and IL-10) and host intestinal growth factors involved in tissue repair (EGF and VEGF). Multimodal imaging is useful for tracking cell sheets and for noninvasive follow-up of their regenerative properties.

Key words: cell sheet technology, image-guided cell therapy, MRI, fluorescence imaging, intestinal fistula.

Introduction

Regenerative medicine has the ultimate goal to overcome the failure of an organ, restoring its function and homeostasis (1). When traditional palliative strategies fail to counteract progressive cellular destruction and loss of functional tissues, regenerative medicine offers new promises in

expanding therapeutic options to address unmet disease management needs (2). In this aim, mesenchymal stem cells (MSCs) represent one of the most well-investigated cell types, being at the frontline of the tissue regeneration juncture. MSCs are multipotent stem cells that can differentiate into a variety of cell types and influence both innate and adaptive immune responses (3). MSCs have received particular attention due to their regenerative and immunomodulatory potentials, as well as their lack of immunogenicity (4,5).

Initial efforts in regenerative medicine relied on the injection of MSCs or other cell types directly into the site of injury (6–8). Despite the hopes, these procedures provided relatively modest improvements in restoring normal structure and function, due to poor cell retention and survival. Indeed, injected cells are often washed out, relocating in off-target organs (9,10), resulting in unsatisfactory engraftment rates. Poor cell retention and survival, and implantation difficulties following cell injection, have motivated the advent of tissue engineering, which combines cells, scaffolds, and growth factors to generate functional and implantable three-dimensional tissues (11). Scaffolds are expected to entrap cells and favor their anchorage at the site of injury, however scaffold biocompatibility and biodegradation remain major concerns (12,13).

Alternatively, scaffold-free strategies have generated increasing interest to reverse organ failure when tissue homeostasis is disrupted. Cell sheet technology consists of the construction of three-dimensional tissues by stacking cell monolayers obtained from temperature-responsive culture surfaces (Figure 1A). Thermosensitive culture supports enable the recovery of cell sheets, preserving intercellular junctions and the extracellular matrix (14). While the intercellular junctions allow cells to form a contiguous monolayer, the extracellular matrix confers bioadhesiveness, prompting cell sheets to adhere on the top of one another to form 3D constructs and to integrate into host tissues without the need for sutures (15). A remarkable advantage of cell sheets compared to scaffold-based strategies is the bypassing of toxic and inflammatory responses elicited by the by-products of scaffold degradation (16). Additionally, cells are readily available to integrate into the host tissue for vessel, heart and liver regeneration (14,17), to name but a few examples. Beyond animal models, cell sheet technology has defined new perspectives in clinical practice. For instance, cell sheet technology showed very encouraging clinical results in many fields such as in cornea repair (15), esophageal stenosis prevention after extended endoscopic mucosal resection for superficial tumor (18), articular cartilage regeneration (19), and in the treatment of severe chronic heart failure due to ischemic heart disease (20,21).

In spite of the promising features, little attention has been focused on conferring cell sheets with imaging properties to monitor the fate of transplanted tissue constructs. A multimodal combination of different imaging techniques – e.g., optical imaging and magnetic resonance imaging – offers the opportunity to profit from the advantages of each modality while minimizing their related limitations in assessing engraftment of the tissue construct, cell fate and therapeutic follow-up. Some reports in the literature focused on dual fluorescent and magnetic labelling of MSCs and other cells for tracking purposes. For instance, Quin *et al* monitored adipose-derived stem cells in a model of mouse carotid artery injury. Green fluorescent protein-expressing cells were labeled with superparamagnetic iron oxide particles enabling cells to be tracked by histological fluorescence analysis and MRI (22). In a related approach, magnetic nanoparticles were coated with flavin mononucleotide for enhancing cell uptake via specific binding to the riboflavin carrier protein and conferring fluorescent properties. Such nanoparticles were successfully used for labelling cells, which enabled their visualization in collagen scaffolds and tissue-engineered vascular grafts by MRI as well as their monitoring cross-validation via optical imaging techniques (23). MRI follow-up and optical imaging validation tracking were equally reported by Salamon *et al* for mouse MSC co-labeled with fluorescent iron oxide micro-particles and carboxyfluorescein succinimidyl ester following the injection into the heart ventricle of healthy mice (24).

Multimodal theranostic scaffold-free approaches could represent a valuable strategy in regenerative medicine to provide new hope for diseases for which current therapeutic approaches have proven to be either ineffective or limited. In particular, abnormal digestive communication between two internal organs, or aberrant organ connection to the skin surface, defined as fistulas, is a life-threatening condition, particularly in patients with multiple comorbidities (25, 26). Digestive fistulas represent a major health problem in subjects with Crohn's disease and patients that have undergone prior gastrointestinal surgery. Fistula management continues to represent a major challenge in clinical practice. Despite significant advances in surgical or conservative techniques and drug treatments (27,28), the healing rate remains unsatisfactory (29).

The aim of the present study was to design bone marrow–derived mesenchymal stem cell (BMMSC)

sheets labeled with fluorescent and magnetic tracers. Dual imaging detection stemmed from the double cargo, providing cell sheets for the first time with multimodal tracking features for preclinical evalulation. The theranostic potential of these magneto-fluorescent stem cell sheets (MFSCS) was assessed in a digestive fistula model in mice. In an image-guided approach, MRI and probe-based confocal laser endomicroscopy (pCLE) were combined to provide both cell tracking and also follow-up of fistula healing. In a comprehensive basis, we also aimed to understand the mechanisms involved in fistula healing. From this standpoint, cells may exert their therapeutic effect via mechanisms either detectable or undetectable by imaging. Respectively, cells may integrate into the host tissue and/or activate molecular mechanisms involved in tissue repair. In order to appraise both effects, imaging was performed and signaling molecules were also investigated. In an integrated view, the relative contribution of each effect has been disclosed herein.

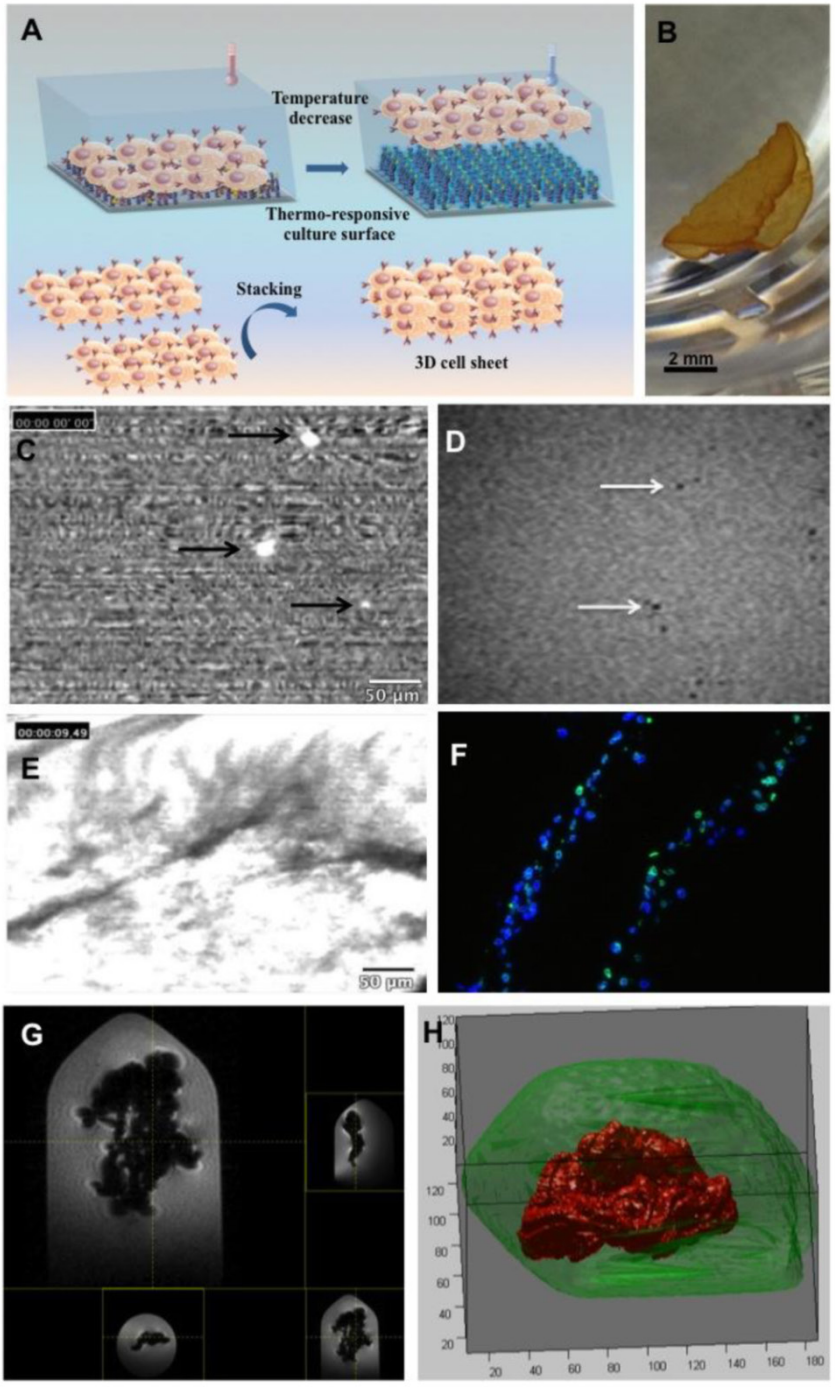

Figure 1: (A) Cell sheet technology: the thermoresponsive culture surface supports cell adhesion and growth at 37°C, while lowering the temperature induces detachment of a cell sheet whose stacking produces a 3D construct. (B) Visual aspect of the magneto-fluorescent stem cell sheet (MFSCS). (C) Optical contrast properties of BMMSCs labeled with both PKH67 fluorescent dye and iron oxide nanoparticles, observed by probe-based confocal laser endomicroscopy. (D) High-resolution MRI analysis of BMMSCs labeled with both PKH67 fluorescent dye and iron oxide dispersed into an agarose gel. (E) 3D construct with intense fluorescence signal. (F) Immunofluorescence images of MFSCS (Dapi and lamin A/C merge). (G) MRI analysis of the labeled stem cell sheet as a whole embedded into an agarose gel. (H) Three-dimensional reconstitution of the labeled cell sheet obtained from MRI data (this reconstitution was performed with a segmentation process based on k-means clustering and morphological filtration. First, filling-filtering was used to exclude (only) dark pixels around the body (air). Then, dark pixels in the body were detected by automated clustering. Matlab (Mathorks,Natick,US) was used for this process.

Material and Methods

Culture of human BMMSCs and magnetic/fluorescent labeling

Human BMMSCs (Lonza, Basel, Switzerland) were cultured in MSCGM complete medium (Lonza, Basel, Switzerland) at 37°C under a 5% CO_2 atmosphere. Fresh medium was replaced every 3 days. BMMSCs between passages 4 to 10 were used in the experiments. For magnetic labeling (30), 8 nm maghemite nanoparticles were used, synthesized by coprecipitation and stabilized in aqueous suspension by adsorption of citrate. These iron oxide nanoparticles (IONP) were dispersed in serum-free RPMI (Roswell Park Memorial Institute) medium (Sigma, France) supplemented with 5 mM citrate at a final iron concentration of 0.1 mM. BMMSCs underwent a 30-minute incubation with this medium at 37°C. Cells were then rinsed twice in serum-free RPMI medium. In order to allow nanoparticle internalization, cells

were incubated for 2 hours with complete medium. Cells were fluorescently labeled with pKH67 green fluorescent dye, following the manufacturer's instructions (Sigma, St. Quentin Fallavier, France), and cultured in complete RPMI medium.

Production of magneto-fluorescent stem cell sheets

Stem cell sheets (SCS) were obtained by culturing BMMSCs, either labeled or not, on commercial thermoresponsive culture plates (UpCell™, CellSeed Inc.). Cells were seeded in 24-well plates (1 million per well) and allowed to adhere in complete culture medium. After 24 hours, confluent cell sheets were then detached by incubating the plate at room temperature for 30 minutes. SCS were harvested as a single contiguous cell layer. SCS were gently aspirated with a pipette and layered on top of one another to obtain a 3D construct.

Murine model of enterocutaneous fistula

Animal experiments were performed in agreement with institutional animal use and care regulations after approval by the local Ethics Committee. Nude NMRI mice (8 weeks old, Janvier-Labs, France) were used. Animals underwent a surgical cecostoma communicating the cecum and the skin under isoflurane anesthesia (Baxter, Maurepas, France) using a SZX10 stereomicroscope (Olympus France SAS, Rungis, France). The cecostoma was performed according the model described by Bultmann and colleagues and this choice was based on the report of no spontaneous stoma closure even four months after surgery (31). After a midline laparotomy of 1 cm, the distal part of the cecum was passed through the abdominal muscle and the subcutaneous space, forming a 1-cm-long tract, and then attached to the skin. Four stitches were made at the site of a 3x3 mm biconcave incision on the left flank of the mouse. Postoperative analgesic treatment was administered for 48 hours (0.5 ml/20 ml acetaminophen diluted in water).

Transplantation of stem cell sheets and follow-up

The transplantation of SCS was carried out three days after surgical fistula creation (Figure 2). A total of 28 mice underwent surgery to create the fistula, without surgical complication. Animals were randomized in two groups: control (n=10) and treated (n=18). Mice were treated with unlabeled SCS (n=10) and dual-labeled SCS (MFSCS) (n=8). Age and weight just before transplantation were comparable between the three groups. At D-3 and D0, clinical examination showed a similar inflammatory feature of the fistula orifice in the three groups. For the transplantation treated group, the BMMSC double layer (2,000,000 cells) with complete medium, either labeled or not, was gently aspirated with a pipette and positioned into the fistula orifice under isoflurane anesthesia. For the control group, the external orifice was cleaned with complete medium only. The inflammatory response at the fistula site was semiquantitatively scored according to erythematous and/or edematous aspect: absent, moderate, or severe.

Mice were followed for 17 days after surgery before sacrifice and histological analysis. MRI and pCLE were performed before and after transplantation, and at D7 and D14.

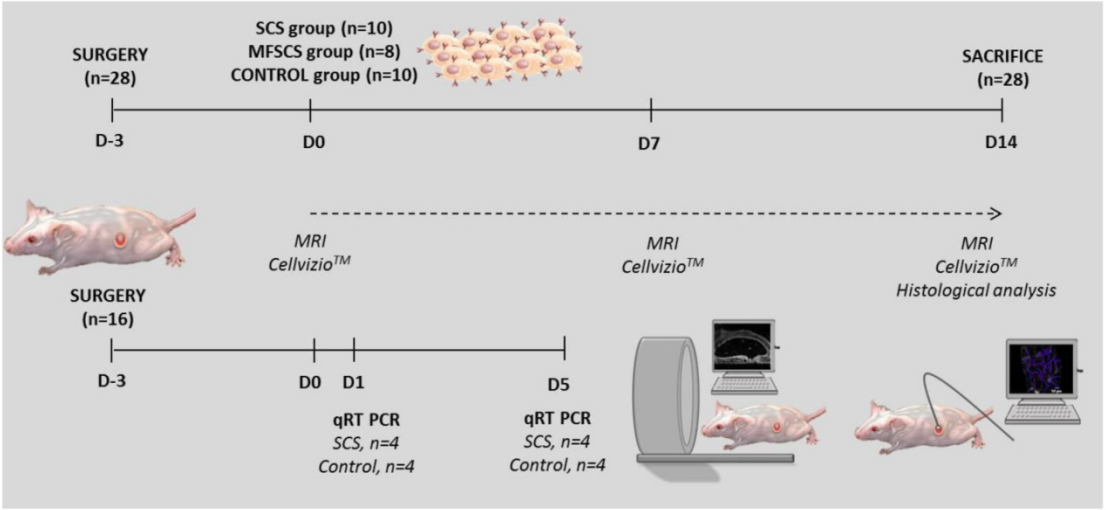

Figure 2: Study protocol (SCS: stem cell sheets; MFSCS: magneto-fluorescent stem cell sheet).

Magnetic resonance imaging (MRI)

MRI was performed using a 4.7 T preclinical MRI scanner (BioSpec 47/40 USR, Bruker, Ettlingen, Germany). The MRI protocol included three types of sequence performed in the three orthogonal planes, with a total acquisition time of 15 minutes per mouse: fast imaging with steady-state precession (FISP) 3D was performed for 3D anatomical location of the fistula, Turbo-rare T2 Fat Sat and FLASH (Table 1).

Table 1: Parameters for MRI image acquisition.

	FISP 3D	Turbo-rare T2 Fat Sat	FLASH
FOV (mm)	13 x 10 x 13	14 x 14	14 x 14
Acquisition matrix	186 x 186 x 143	256 x 256	256 x 256
Resolution (mm/pixel)	0.070 x 0.054 x 0.091	0.055 x 0.055	0.55 x 0.55
Echo time (ms)	3.603	15.650	2.6
Repetition time	16.865	4000	60
Flip angle (degree)	25	-	90

For the *in vitro* investigation, 0.3% low-melting-point agarose gels were spiked with magneto-fluorescent BMMSCs. Alternatively, the whole labeled cell sheet was embedded in the gel.

Animals were placed under isoflurane anesthesia and breathing was monitored. All MRI images were analyzed by two investigators (one experienced radiologist and one trained gastroenterologist), blinded to treatment allocation.

The first objective was to track the labeled cells. To this end, a cryogenic probe (Cryoprobe™, Bruker) was used for high resolution.

The second objective was to evaluate the fistula healing by measuring the fistula orifice with the software, Paravision 5.1, JIVE tool (Bruker), in the three orthogonal planes (Figure S1). This enabled the delimitation of the fistula orifice surface as a region of interest (ROI), for which the size was calculated (cm^2).

Probe-based confocal laser endomicroscopy (pCLE)

A probe-based confocal laser endomicroscopy device, Cellvizio™ (Mauna Kea Technologies, France), was used under isoflurane anesthesia first for cellular tracking and second for microvascular network assessment at the fistula site. The device was equipped with a flexible fiber optic miniprobe, which works as a microscope objective (1.8 mm diameter, 3.5 µm spatial resolution, 12 images per second acquisition). pCLE was performed under isoflurane anesthesia. The probe was positioned in direct contact with the transplantation site. The region of the fistula and its periphery were analyzed thoroughly. The probe was introduced into the fistula as far as the size of the orifice allowed for miniprobe insertion. Labeled cells were visualized as bright dots, notably different from the digestive liquid (diffuse background with low brightness) and the animal hair (filament-like fluorescent signal). The density of the microvascular network at the transplantation site and its periphery was also investigated by pCLE after the intravenous administration of FITC-dextran 70 kDa. Mosaicing™ software (Mauna Kea Technologies, France) was employed to enable a real-time display of the draft mosaic gathering the acquired and previous images. A dedicated module, Vessel Detection™ (Mauna Kea Technologies, France), was used to compute the functional capillary density (FCD) and diameter distribution. A diameter of interest (DOI) of 4 µm was chosen to avoid underestimation of small vessels that are the most important in tissue regeneration. The pCLE analysis was carried out at D0 (transplantation time point), D7, and D14.

Polymerase chain reaction (PCR)

Sixteen additional mice were sacrificed on days 1 and 5 after transplantation (n=4 for each time point and group). The fistula was collected (1 cm^3 in size) and intestinal tissue was isolated. Total RNA was extracted from the intestine using the Trizol reagent according to the manufacturer's instructions (Invitrogen, Paris, France). RNA quality was assessed on a denaturing agarose gel (1%) stained with ethidium bromide. After RNA extraction, 1 µg was reverse transcribed to cDNA with the QuantiTect Reverse Transcription kit (Qiagen, Hilden, Germany). Quantitative reverse transcription polymerase chain reaction (RT-qPCR) was performed with Taqman gene expression assays for proinflammatory factors (IL-6, IL-8, IL-1ß, TNFα: tumor necrosis factor α), anti-inflammatory factors (IL-10, TGF-ß2: transforming growth factor ß2, IL-35), chemotactic factors (MIP-1 alpha: macrophage inflammatory protein 1 alpha, RANTES: regulated on activation, normal T cell expressed and secreted), growth factors (VEGF: vascular endothelial growth factor, EGF: epidermal growth factor, ILC: innate lymphoid cell, IL-22, amphiregulin) with Taqman Universal PCR master mix using a CFX-96 (Bio-Rad, France). cDNA samples were duplicated and expression was normalized relative to the mouse hypoxanthine phosphoribosyltransferase (HPRT) gene with ΔΔCT calculation. The mRNA levels of genes of interest (R) were expressed relative to levels of HPRT (ΔCT = CT(R) – CT (HPRT)) and the relative amount of R mRNA levels between BMMSC and Control was given by ΔΔCT, where ΔΔCT = [ΔCT (R) of BMMSC] - [ΔCT(R) of control] for the same time point. In a second step, the protocol was tested using the human

housekeeping gene (RPLPO: Large Ribosomal Protein) prior to evaluation of the various other human factors.

Histological examination

At D14, mice were sacrificed and the fistula site and its periphery (1 cm^3 specimen) were collected and embedded in Tissue-Tek Optimal Temperature Cutting medium (Sakura, Torrance, CA) and frozen in liquid nitrogen. Specimens were first sectioned perpendicular to the center of the fistula and then the two fragments obtained were fully sectioned to obtain thin tissue sections of 7 µm, which were stained with hematoxylin and eosin (HE), Perl's stain for intracellular iron assessment, and Sirius Red for measurement of fibrosis. A total of 240 sections at different levels were obtained from each fistula. Slices were analyzed with an optical and fluorescence microscope (Leica DMIL) equipped with a digital camera (Qicam, Qimaging, Burnaby, BC, Canada). Two investigators, blinded to treatment allocation, performed histological analyses. All slides were digitally scanned (Digitiser Hamamatsu Photo-nics®, Massy, France) and analyzed with dedicated software ((NDP.view software®, Massy, France).

Measurement of fibrosis infiltration and fistula orifice

For each mouse, all the sagittal tissue sections passing through the center of the fistula and showing the maximal fibrosis infiltration were analyzed. The center of the fistula was defined by the visualization, on the same slide, of the skin in continuity with the fistula tract and finally the intestinal epithelium.

Fibrosis surface (mm^2) and maximal size of the fistula orifice (µm) were measured at 1.25x magnification in the slide passing through the center of the fistula (HE staining).

Assessment of human BMMSCs

Transplanted human cells were detected using an antibody directed against human specific nuclear protein lamin A/C (Novocastra, Newcastle upon Tyne, UK) diluted at a ratio of 1:300 in PBS containing bovine serum albumin (2%). The specific binding of primary antibodies was revealed with FITC secondary antibodies. 4,6-diamino-2-phenylindole (DAPI, SIGMA) was used to identify nuclei.

Statistics

The results are presented as means ± standard deviation for continuous variables, and as percentages for categorical variables. GraphPadPrism (Graphpad Software, La Jolla, CA, USA) software was used for statistical analyses. Fischer's exact test was carried out for comparisons between categorical variables and the nonparametric Mann-Whitney test was used for nonpaired continuous variables. Comparisons between more than two groups were performed with the nonparametric Kruskal-Wallis test. Dunn's multiple comparison test difference in rank sum was used for pairwise comparison. A p-value of less than 0.05 was considered statistically significant.

Results and Discussion

Designing stem cell sheets

Stem cell sheets were produced from monolayers of cells labeled with PKH67 fluorescent dye and iron oxide nanoparticles. Concerning the magnetic labeling protocol, this confers a 3 pg iron load per cell in the case of BMMSCs (32, 33). It is important to highlight that the impact of magnetic nanoparticle uptake by BMMSCs has already been assessed. The dose-dependent effect on cell differentiation was determined and a safe threshold up to 10 pg iron per cell was demonstrated (32, 33).

Magneto-fluorescent stem cell sheets were harvested at room temperature from thermoresponsive culture supports (Figure 1B). Two cell sheets were stacked on top of one another to form a hybrid 3D cell sheet.

The contrast properties of BMMSCs with both PKH67 fluorescent dye and iron oxide nanoparticles were tested *in vitro*. pCLE images of labeled cells evidenced bright fluorescent spots indicating successful detection by optical microscopy (Figure 1C). High-resolution MRI analysis enabled the detection of individual cells dispersed in an agarose gel. Labeled BMMSCs were visualized as hypointense spots distributed throughout the gel (Figure 1D). The contrast properties of the MFSCS were analyzed by MRI. The labeled stem cell sheet was visualized as a large hyposignal on T2-weighted imaging (Figure 1E). A three-dimensional reconstitution of the cell sheet, based on MRI data, is provided in Figure 1F.

Fistula model

The fistula model allowed the reproduction of a structure closely resembling a digestive fistula with skin and intestinal lesions and the continuous passage of digestives secretions. There was no complication related to fistula induction surgery. To date, apart from the present study and that of Bultmann and colleagues (31), no other fistula model, either in mice or in any other animal, has been reported in the literature.

Imaging: Probe-based confocal laser endomicroscopy

pCLE provided information on cell tracking and on vascularization status at the injury site. pCLE cell

tracking was performed at D0, D7 and D14 (Figure 3A-C). At D0, pCLE analysis showed intense fluorescence signal at the transplantation site after grafting for mice treated with MFSCS (Figure 3A), while no signal was observed for unlabeled SCS. At D7, only two mice treated with MFSCS presented a fluorescence signal superior to the controls. Follow-up of the fluorescent signal in these two mice showed a rapid decrease after the first 72 hours. At D14, the fluorescence signal level was very low and similar for control mice and mice treated with MFSCS.

Concerning the assessment of vascularization status, pCLE showed that transplantation of MFSCS enhanced microvascularization at the fistula site while notably promoting fistula healing. Microvasculature analysis by pCLE was carried out for four mice treated with MFSCS and five control mice. Mice from the MFSCS group presented a dense, thin capillary network at the periphery of the fistula orifice at D14 (Figure 3D). There was no fluorescein leakage. Conversely, control animals presented vessels with a wider diameter (Figure 3E). Fluorescein leakage was more frequently observed and a reduced capillary network density was demonstrated. The density of the microvasculature was significantly higher in the MFSCS group in comparison with control mice (p=0.015) (Figure 3F). The effectiveness of pCLE to evaluate microvascularization in an inflammatory situation (inflammatory bowel disease or cancer) has already been published (34, 35).

Imaging: MRI

In our study, MRI allowed confirmation of the location of the MFSCS in the fistula orifice and assessment of the reduction of the fistula orifice surface.

At D0, MFSCS were visualized on T2-weighted imaging as a large hyposignal inside the fistula (Figure 4). Unlabeled SCS and controls did not show any modification of the fistula appearance after the procedure (Table S1). At D7 and D14, the MRI appearance of the fistula was more complex. In the MFSCS group, large hyposignal areas were no longer visible. Some smaller hyposignal regions however remained visible and these were more frequent in the MFSCS group compared with the unlabeled SCS and control groups. The occurrence of hyposignal regions in unlabeled SCS and control mice may be associated with air-liquid susceptibility artifacts.

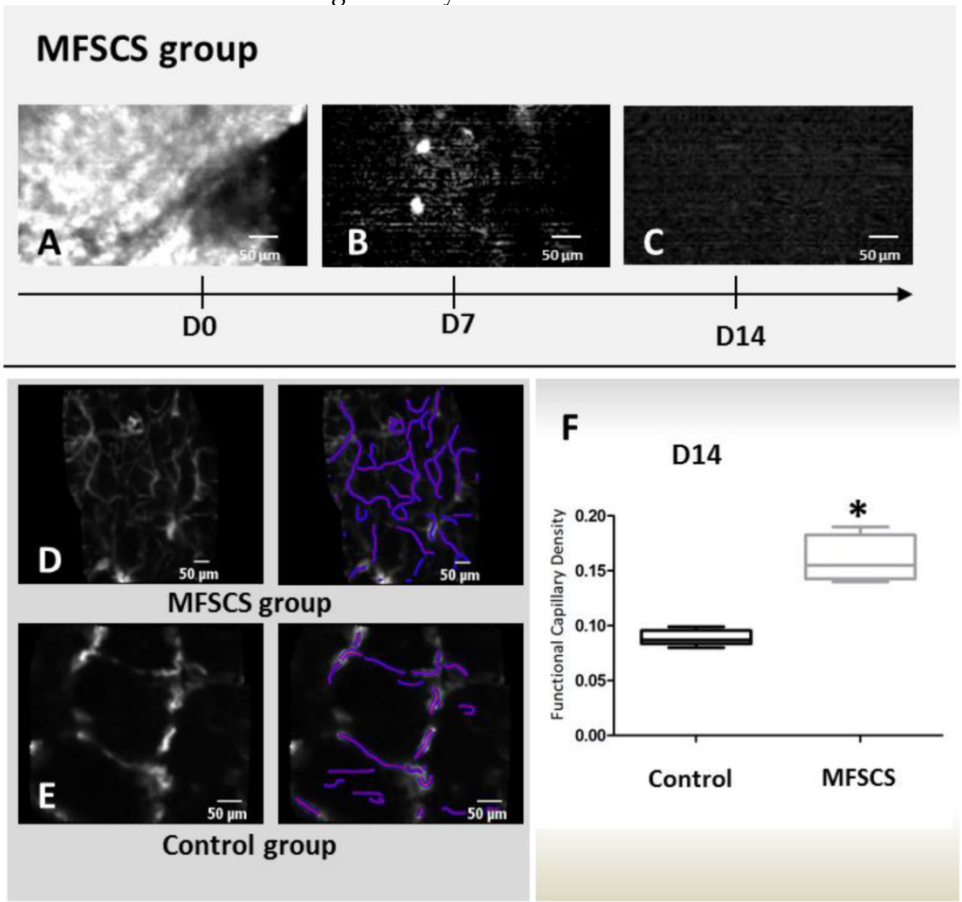

Figure 3: Probe-based confocal laser endomicroscopy (pCLE) at D0 at the fistula site for mice treated with magneto-fluorescent stem cell sheets (MFSCS) showed intense fluorescence signal at the transplantation site (A), which was greatly decreased at D7 (B) and D14 (C). pCLE to investigate microvasculature at D14: mice from the MFSCS group presented a dense thin capillary network at the periphery of the fistula orifice (D). The control group showed fewer vessels, which presented a wider diameter (E). The density of the microvasculature was calculated with a dedicated module, Vessel Detection™ (Mauna Kea Technologies, France) (F).

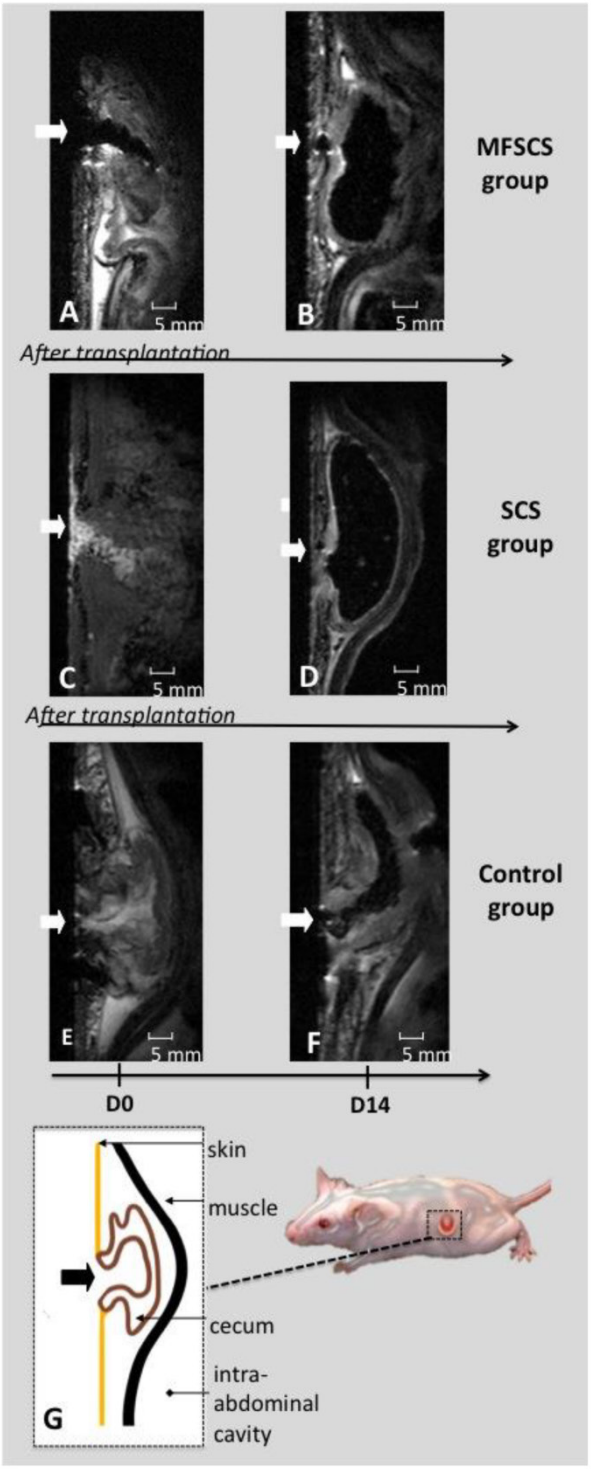

Figure 4: MRI analysis (Turbo rare T2) at the site of the fistula (arrow) on sagittal views from grafted and control mice. Magneto-fluorescent stem cell sheets (MFSCS) immediately after transplantation (A) and at D14 (B). Stem cell sheet (SCS) immediately after transplantation (C) and at D14 (D). Control mouse at D0 (E) and D14 (F). The grafted MFSCS could be visualized as an intense hyposignal at D0 (A). Hyposignal artefacts could be visualized both for control (F) and grafted (B: MFSCS and D: SCS) mice. Schematic representation of the fistula structure (G).

Regarding measurement of the fistula surface, at D14, the median fistula orifice surface was smaller in treated mice (2.2±1.1 mm^2 for SCS and 3.2±1.1 mm^2 for MFSCS) in comparison with controls (5.6±1.2 mm^2). This corresponded to a decrease in the surface from D0 to D14 of 72.2% for SCS and 62.9% for MFSCS. In control animals, the decrease was only 31.7% (Figure S1). The comparison between the treated groups (SCS and MFSCS) and control group represented a statistically significant difference ($p<0.001$), whereas no statistically significant difference was observed between SCS and MFSCS ($p=0.73$).

Magnetic labelling was performed with an iron oxide intracellular concentration of 3 pg (Fe). Previous investigations at a 10 pg intracellular concentration revealed minimal impact on endothelial cell viability and function (36) as well as on MSC proliferation, metabolic function and differentiation (33). However, non labelled cells seem to induce an improved therapeutic effect compared to labeled ones. Even if this difference is not statistically significant, a mixture of labelled and non labelled cells may be a valuable strategy for future work, also considering that there is a too high MRI signal leading to blooming effects in some analyses.

The role of signaling molecules

The therapeutic contribution of cells may involve mechanisms undetectable by imaging. In order to bridge this gap, signaling molecules were also investigated. Considering that the aim was to seek for the intrinsic cell therapy impact on signaling molecules involved in healing, this investigation was conducted following treatment with non-labelled cell sheets. We also consider performing the analysis of signaling molecules for a mix labeled and unlabeled cells sheets in future work.

Endogenous expression of EGF and VEGF, growth factors involved in tissue repair processes at the fistula site, was upregulated in treated compared with control mice. This difference was statistically significant at D5 and there was a significant increase in EGF and VEGF mRNA between D1 and D5 in grafted SCS mice ($p=0.007$ and $p=0.045$, respectively) and not in control mice (Figure 5). Evolution analysis of factors between D1 and D5 showed a significant increase in the synthesis of anti-inflammatory factors, such as TGF-ß2 and IL-10, in grafted SCS mice ($p=0.008$ and $p=0.033$, respectively) compared with control mice. Although not statistically significant, the synthesis of IL-6 was higher at D5 in SCS mice. There was no difference for the proinflammatory factors, TNF-alpha and IL-8, between control and SCS groups. The mRNA level of the chemotactic factor, MIP-1alpha, tended to be increased in SCS mice, but the difference was not statistically significant (Figure S2 and Table S2). Human RPLPO mRNA was not detected in any of the intestinal specimens at D1 and D5 (data not shown).

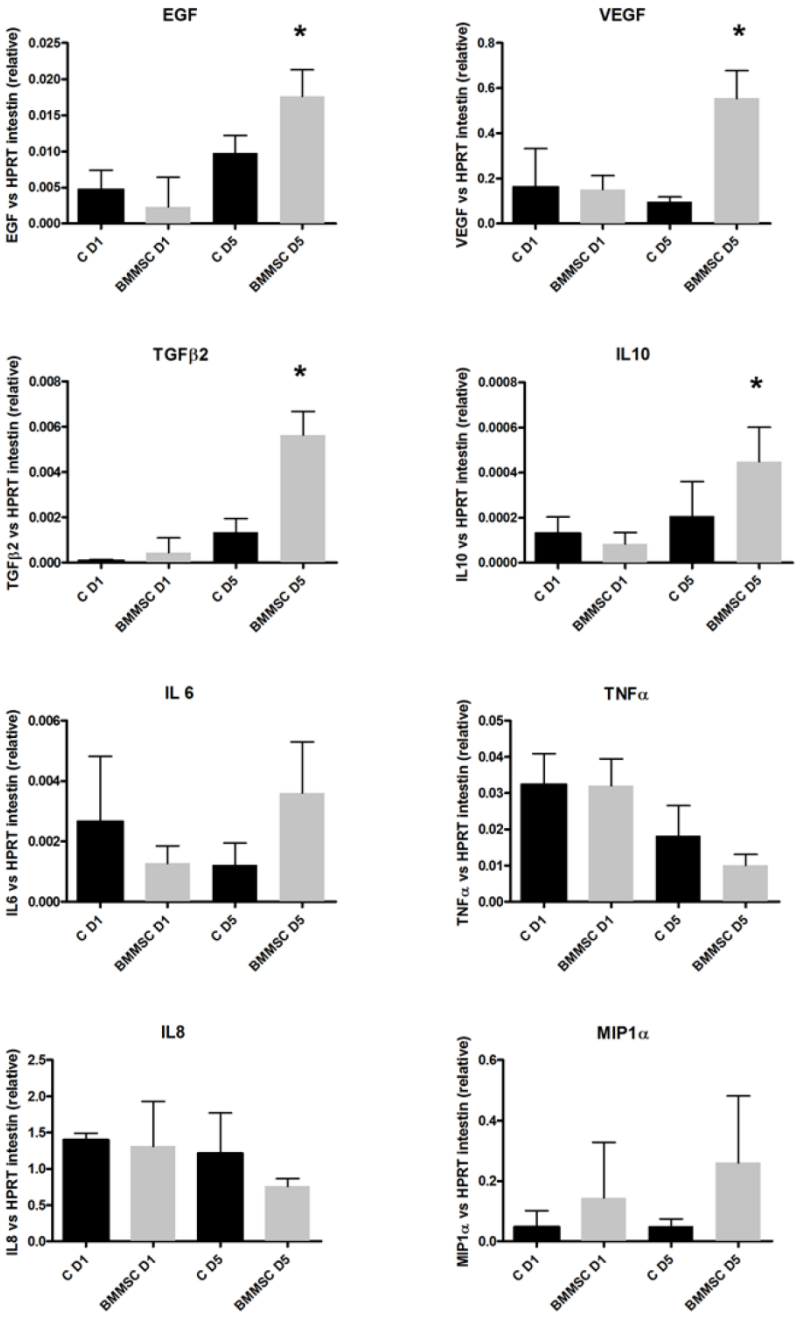

Figure 5: Chemokine factor profile in the intestinal mucosa of treated and control mice at D1 and D5. Results are presented as ΔΔCT for 8 cytokines comparing the relative qRT-PCR values in the fistulas of control and mice treated with bone marrow–derived mesenchymal stem cell (BMMSC) sheets at day 1 (D1) and day 5 (D5) after grafting. qRT-PCR values were normalized by those of mouse (HPRT) gene (individual values are given in Table S3).

These results indicate that the grafted SCS construct interplays with endogenous mechanisms of repair, leading to an upregulated expression of host trophic factors. Such interaction with endogenous reparative mechanisms has been reported in the literature previously. Indeed, intramuscular MSC injections were found to induce a global trophic effect resulting in elevated host tissue growth factor levels (37, 38).

Preclinical evaluation

No mouse lost weight, and weight gain from D-3 to D14 was similar between the three groups (control: 5.3 g ±1.06; SCS: 5.97 g ±0.98, MFSCS: 5.58 g ±1.05).

There were two cases of complete fistula healing in treated mice (one for SCS and one for MFSCS). The fistula orifice evolved to a dot-shaped orifice in 50% of mice grafted with MFSCS, 60% of mice grafted with SCS, and in none of the mice in the control group (Figure 6). Clinical evaluation at D14 indicated that

60% (6/10) of the control group presented an inflammatory orifice fistula, while inflammation was present in only 17% of mice (3/18) in the SCS plus MFSCS groups.

In this preclinical investigation, the choice of BMMSCs was based on their ability to differentiate and transdifferentiate into tissue-specific cells and their low inherent immunogenicity (39). Indeed, the transplantation of BMMSCs expanded *ex vivo* has been found to improve tissue repair of infarcted heart (40) and brain (41) in animals. Both adipose tissue–derived stem cells (ADSCs) and BMMSCs have been successfully used to treat fistulas in human trials in the case of Crohn's disease in some reports (42–44). Cell sheets have been used to prevent stenosis after extended endoscopic submucosal dissection in animals and in humans, with excellent results (45,18). However, there was little evidence regarding stem cell therapy for patients with digestive fistulas, and the cell sheet approach has never been transposed to fistula treatment.

Histology

Histological analyses validated imaging and clinical evaluation data. The histological analysis of HE-stained tissue sections enabled the discrimination of fistula structures featuring a dermal layer, subcutaneous abdominal muscle and part of the digestive tract (Figure 7). Complete healing was evidenced for two treated mice by a continuous tissue layer at the fistula site, confirming MRI data. The fibrosis infiltration surface at the tissue surrounding the fistula orifice site was higher in the control group in comparison with the treated group (Table S3). The maximal size of the fistula orifice was also larger in the control than SCS group. Perl's staining for intracellular iron assessment was positive in four treated mice in the MFSCS group. One mouse in each of the control and unlabeled SCS groups was also positive at the fistula site, which could account for the presence of blood at the surgical site.

Concerning immunofluorescence analysis, nuclear lamin A/C characteristic of human cells could not be detected at the fistula site of treated mice, although staining was positive *in vitro* prior to grafting.

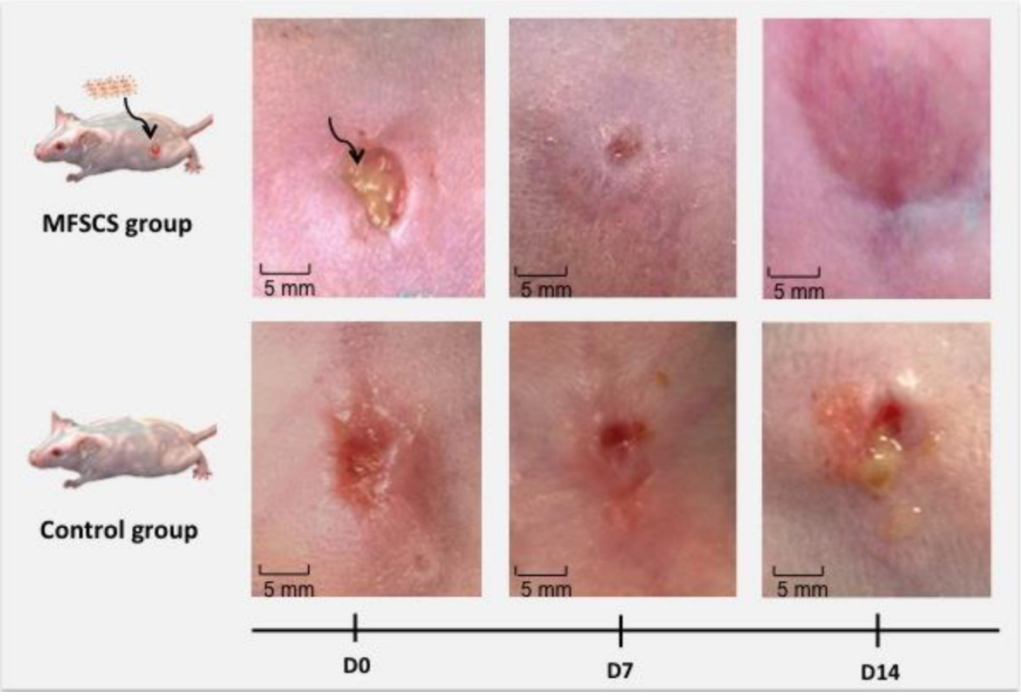

Figure 6: Preclinical aspect of the fistula at D0, D7 and D14 in representative grafted mice. At D0 in the MFSCS group, an arrow shows the cell sheet placed within the fistula. At D14 in the MFSCS group, the fistula showed a drastic healing with closure of the external orifice.

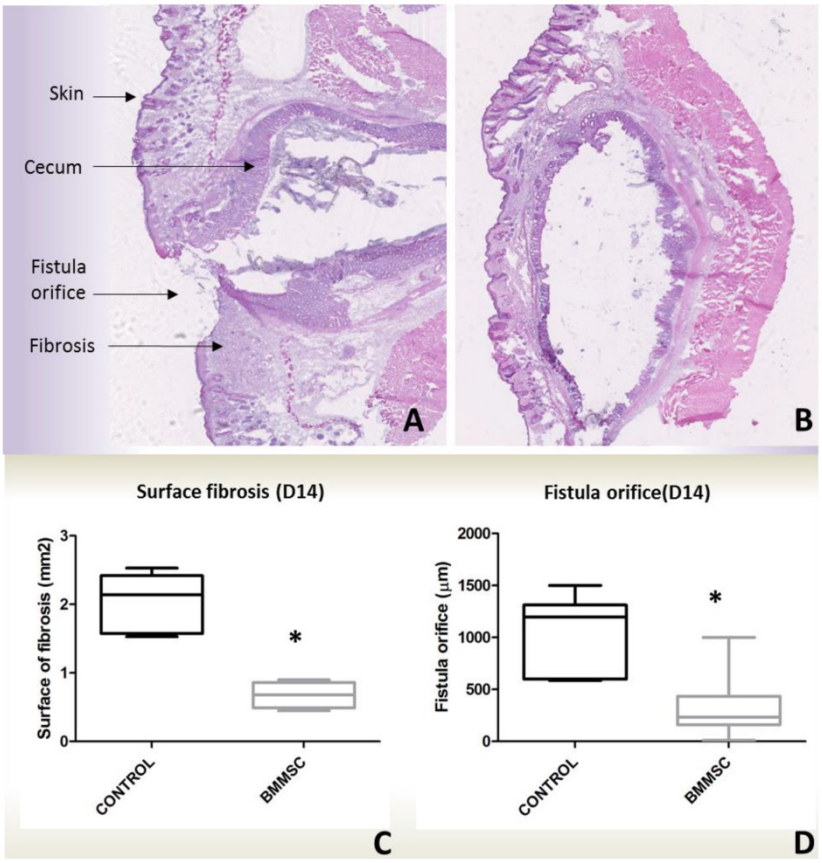

Figure 7: Histological analysis of HE-stained tissue sections (1.25x) passing through the center of the fistula for a control mouse (A), and a bone marrow–derived mesenchymal stem cell (BMMSC) sheet–treated mouse with complete closure (B). In comparison with control mice, the area of surface fibrosis (C) and the fistula orifice (D) were smaller in treated mice.

Image-guided therapy: an integrated preclinical and clinical view

Considering the preclinical set-up, when proposing an innovative cell therapy strategy, cell labelling is needed to validate the appropriate graft positioning as well as to enable longitudinal follow-up. For instance in an image-guided approach, the clinician would benefit from information on the implantation site of the graft enabling to rectify the surgical act in case of poor graft positioning or immediate graft migration. From this standpoint, the clinicians need accurate information from imaging modalities combining both sensitivity, resolution and anatomical information. In this regard, multi-modal imaging represents an important tool considering that each imaging modality has unique strengths along with intrinsic limitations. A multi-modal combination of different imaging techniques offers the opportunity to take profit from the advantages of each modality while minimizing their related limitations in a complementary basis (46). Our choice was to use optical imaging for its versatility and sensitivity and compensate its poor resolution and depth limitation by coupling magnetic resonance imaging (MRI), which additionally provided anatomical information. In order to do this, we used a lipophilic membrane dye and iron oxide magnetic nanoparticles. PKH lipophilic dyes are able to stably, brightly, and homogeneously label a wide range of cell types (47) while iron oxide nanoparticles are widely used biocompatible and biodegradable MRI contrast agents already approved by the FDA (48). PKH dyes stain the cell membrane while iron oxide nanoparticles label cell endosomal/lysomal compartments. Although the combination of these labelling/imaging strategies may provide informative data on graft implantation and its longitudinal follow-up, the clinician must be aware about the existing limitations such as the dilution of the labelling agent following cell division and its unspecific transfer to bystander cells, which may mislead cell tracking. For instance, it has been demonstrated that cells stained with dual PKH and magnetic nanoparticles may release extracellular vesicles that sequestrate both labeling agents transferring them to naïve cells, which in turn become double labelled (49,50).

Considering cell tracking difficulties, the use magnetic and fluorescent labelling and MRI coupled to optical imaging to follow the fate of grafted cells

still seems difficult to be implemented in the clinical practice, although it is of great interest. However, we anticipate that such multimodal imaging strategy may find its way in the clinical set-up for following-up therapeutic outcome in fistula treatment via orifice assessment and angiogenesis evaluation.

Conclusions

To the best of our knowledge, this is the first time that stem cell sheets combining magnetic and fluorescent features have been designed for precliniclal evaluation. Herein, dual imaging detection stemmed from this double cargo unprecedentedly providing cells sheets with multimodal tracking features. In an image-guided approach, MRI/optical multimodal imaging allowed MFSCS tracking, as validated by histological Perl's staining. Multimodal imaging also enabled follow-up of SCS therapeutic outcome, indicating fistula orifice closure (MRI) and proangiogenic response (pCLE). Clinical, radiological, and histological analyses converged to attest improved fistula healing in SCS- and MFSCS-treated mice compared with controls. Importantly, magneto-fluorescent labeling minimally affected the regenerative properties of the stem cell sheets. SCS engraftment induced a higher level of expression of endogenous growth factors involved in tissue reparation and of anti-inflammatory cytokines. The results obtained indicate that SCS concurrently contribute to fistula healing by direct integration into the host tissue and by indirect upregulation of host trophic factor expression. The pioneer approach proposed herein opens up new prospects in cell sheet tracking. It resonates with the current need of regenerative medicine for noninvasive imaging methods to monitor the fate of transplanted tissues in preclinical approaches, while encompassing follow-up of therapeutic outcome.

Supplementary Material

Supplementary tables and figures.
http://www.thno.org/v06p0739s1.pdf

Acknowledgments

This work was supported by ENCITE, co-funded by the European Commission under the 7th Framework Programme.

We sincerely thank Sophie Camilleri-Broet (Department of Pathology, Hôpital Européen Georges Pompidou, Paris, France) for her assistance in the field of histology; Josette Legagneux (Microsurgery Training and Research Lab, School of Surgery, Paris, France) for her great advice in the field of microsurgery, and Nicolas Guegan (Institut IMAGINE-INSERM 1163, Paris, France) for his technical assistance.

Competing Interests

The authors have declared that no competing interest exists.

References

1. O'Brien FJ. Biomaterials & scaffolds for tissue engineering. Mater Today. 2011;14(3):88-95.
2. Nelson TJ, Martinez-Fernandez A, Yamada S, Ikeda Y, Perez-Terzic C, Terzic A. Induced pluripotent stem cells: advances to applications. Stem Cells Cloning Adv Appl. 2010;3:29-37.
3. Krampera M, Pasini A, Pizzolo G, Cosmi L, Romagnani S, Annunziato F. Regenerative and immunomodulatory potential of mesenchymal stem cells. Curr Opin Pharmacol. 2006;6(4):435-41.
4. Nauta AJ, Fibbe WE. Immunomodulatory properties of mesenchymal stromal cells. Blood. 2007;110(10):3499-506.
5. Satija NK, Singh VK, Verma YK, Gupta P, Sharma S, Afrin F, et al. Mesenchymal stem cell-based therapy: a new paradigm in regenerative medicine. J Cell Mol Med. 2009;13(11-12):4385-402.
6. Menasché P, Hagège AA, Scorsin M, Pouzet B, Desnos M, Duboc D, et al. Myoblast transplantation for heart failure. Lancet Lond Engl. 2001;357(9252):279-80.
7. Assmus B, Honold J, Schächinger V, Britten MB, Fischer-Rasokat U, Lehmann R, et al. Transcoronary transplantation of progenitor cells after myocardial infarction. N Engl J Med. 2006;355(12):1222-32.
8. Lunde K, Solheim S, Aakhus S, Arnesen H, Abdelnoor M, Egeland T, et al. Intracoronary injection of mononuclear bone marrow cells in acute myocardial infarction. N Engl J Med. 2006;355(12):1199-209.
9. Zhang H, Song P, Tang Y, Zhang X, Zhao S, Wei Y, et al. Injection of bone marrow mesenchymal stem cells in the borderline area of infarcted myocardium: heart status and cell distribution. J Thorac Cardiovasc Surg. 2007;134(5):1234-40.
10. Hale SL, Dai W, Dow JS, Kloner RA. Mesenchymal stem cell administration at coronary artery reperfusion in the rat by two delivery routes: a quantitative assessment. Life Sci. 2008;83(13-14):511-5.
11. Langer R, Vacanti JP. Tissue engineering. Science. 1993;260(5110):920-6.
12. Haraguchi Y, Shimizu T, Yamato M, Okano T. Concise review: cell therapy and tissue engineering for cardiovascular disease. Stem Cells Transl Med. 2012;1(2):136-41.
13. Soler-Botija C, Bagó JR, Bayes-Genis A. A bird's-eye view of cell therapy and tissue engineering for cardiac regeneration. Ann N Y Acad Sci. 2012;1254:57-65.
14. Masuda S, Shimizu T, Yamato M, Okano T. Cell sheet engineering for heart tissue repair. Adv Drug Deliv Rev. 2008;60(2):277-85.
15. Nishida K, Yamato M, Hayashida Y, Watanabe K, Yamamoto K, Adachi E, et al. Corneal reconstruction with tissue-engineered cell sheets composed of autologous oral mucosal epithelium. N Engl J Med. 2004;351(12):1187-96.
16. Miyagawa S, Roth M, Saito A, Sawa Y, Kostin S. Tissue-engineered cardiac constructs for cardiac repair. Ann Thorac Surg. 2011;91(1):320-9.
17. Harimoto M, Yamato M, Hirose M, Takahashi C, Isoi Y, Kikuchi A, et al. Novel approach for achieving double-layered cell sheets co-culture: overlaying endothelial cell sheets onto monolayer hepatocytes utilizing temperature-responsive culture dishes. J Biomed Mater Res. 2002;62(3):464-70.
18. Ohki T, Yamato M, Ota M, Takagi R, Murakami D, Kondo M, et al. Prevention of esophageal stricture after endoscopic submucosal dissection using tissue-engineered cell sheets. Gastroenterology. 2012;143(3):582-8.e1-2.
19. Sato M, Yamato M, Hamahashi K, Okano T, Mochida J. Articular cartilage regeneration using cell sheet technology. Anat Rec Hoboken NJ 2007. 2014;297(1):36-43.
20. Sawa Y, Yoshikawa Y, Toda K, Fukushima S, Yamazaki K, Ono M, et al. Safety and Efficacy of Autologous Skeletal Myoblast Sheets (TCD-51073) for the Treatment of Severe Chronic Heart Failure Due to Ischemic Heart Disease. Circ J Off J Jpn Circ Soc. 2015;79(5):991-9.
21. Imamura T, Kinugawa K, Sakata Y, Miyagawa S, Sawa Y, Yamazaki K, et al. Improved clinical course of autologous skeletal myoblast sheet (TCD-51073) transplantation when compared to a propensity score-matched cardiac resynchronization therapy population. J Artif Organs Off J Jpn Soc Artif Organs. 2015.
22. Qin J-B, Li K-A, Li X-X, Xie Q-S, Lin J-Y, Ye K-C, et al. Long-term MRI tracking of dual-labeled adipose-derived stem cells homing into mouse carotid artery injury. Int J Nanomedicine. 2012;7:5191-203.
23. Mertens ME, Frese J, Bölükbas DA, Hrdlicka L, Golombek S, Koch S, et al. FMN-Coated Fluorescent USPIO for Cell Labeling and Non-Invasive MR Imaging in Tissue Engineering. Theranostics. 2014;4(10):1002-13.
24. Salamon J, Wicklein D, Didié M, Lange C, Schumacher U, Adam G, et al. Magnetic resonance imaging of single co-labeled mesenchymal stromal cells

after intracardial injection in mice. RöFo Fortschritte Auf Dem Geb Röntgenstrahlen Nukl. 2014;186(4):367-76.
25. Burgos AM, Braghetto I, Csendes A, Maluenda F, Korn O, Yarmuch J, et al. Gastric leak after laparoscopic-sleeve gastrectomy for obesity. Obes Surg. 2009;19(12):1672-7.
26. Stroh C, Birk D, Flade-Kuthe R, Frenken M, Herbig B, Höhne S, et al. Results of sleeve gastrectomy-data from a nationwide survey on bariatric surgery in Germany. Obes Surg. 2009;19(5):632-40.
27. Tozer PJ, Burling D, Gupta A, Phillips RKS, Hart AL. Review article: medical, surgical and radiological management of perianal Crohn's fistulas. Aliment Pharmacol Ther. 2011;33(1):5-22.
28. Cho JH. The genetics and immunopathogenesis of inflammatory bowel disease. Nat Rev Immunol. 2008;8(6):458-66.
29. Kumar N, Thompson CC. Endoscopic therapy for postoperative leaks and fistulae. Gastrointest Endosc Clin N Am. 2013;23(1):123-36.
30. Massart R, Dubois E, Cabuil V, Hasmonay E. Preparation and properties of monodisperse magnetic fluids. J Magn Magn Mater. 1995;149(1–2):1-5.
31. Bültmann O, Philipp C, Ladeburg M, Berlien HP. Creation of a caecostoma in mice as a model of an enterocutaneous fistula. Res Exp Med Z Für Gesamte Exp Med Einschl Exp Chir. 1998;198(4):215-28.
32. Fayol D, Luciani N, Lartigue L, Gazeau F, Wilhelm C. Managing magnetic nanoparticle aggregation and cellular uptake: a precondition for efficient stem-cell differentiation and MRI tracking. Adv Healthc Mater. 2013;2(2):313-25.
33. Fayol D, Frasca G, Le Visage C, Gazeau F, Luciani N, Wilhelm C. Use of magnetic forces to promote stem cell aggregation during differentiation, and cartilage tissue modeling. Adv Mater Deerfield Beach Fla. 2013;25(18):2611-6.
34. Kiesslich R, Duckworth CA, Moussata D, Gloeckner A, Lim LG, Goetz M, et al. Local barrier dysfunction identified by confocal laser endomicroscopy predicts relapse in inflammatory bowel disease. Gut. 2012;61(8):1146-53.
35. Fitoussi V, Faye N, Chamming's F, Clement O, Cuenod C-A, Fournier LS. In vivo imaging of tumor angiogenesis using fluorescence confocal videomicroscopy. J Vis Exp JoVE. 2013;(79).
36. Di Corato R, Gazeau F, Le Visage C, Fayol D, Levitz P, Lux F, et al. High-resolution cellular MRI: gadolinium and iron oxide nanoparticles for in-depth dual-cell imaging of engineered tissue constructs. ACS Nano. 2013;7(9):7500-12.
37. Shabbir A, Zisa D, Lin H, Mastri M, Roloff G, Suzuki G, et al. Activation of host tissue trophic factors through JAK-STAT3 signaling: a mechanism of mesenchymal stem cell-mediated cardiac repair. Am J Physiol Heart Circ Physiol. 2010;299(5):H1428-38.
38. Cho H-J, Lee N, Lee JY, Choi YJ, Ii M, Wecker A, et al. Role of host tissues for sustained humoral effects after endothelial progenitor cell transplantation into the ischemic heart. J Exp Med. 2007;204(13):3257-69.
39. Li H, Fu X. Mechanisms of action of mesenchymal stem cells in cutaneous wound repair and regeneration. Cell Tissue Res. juin 2012;348(3):371-7.
40. Amado LC, Saliaris AP, Schuleri KH, St John M, Xie J-S, Cattaneo S, et al. Cardiac repair with intramyocardial injection of allogeneic mesenchymal stem cells after myocardial infarction. Proc Natl Acad Sci U S A. 2005;102(32):11474-9.
41. Li Y, Chen J, Zhang CL, Wang L, Lu D, Katakowski M, et al. Gliosis and brain remodeling after treatment of stroke in rats with marrow stromal cells. Glia. 2005;49(3):407-17.
42. Ciccocioppo R, Bernardo ME, Sgarella A, Maccario R, Avanzini MA, Ubezio C, et al. Autologous bone marrow-derived mesenchymal stromal cells in the treatment of fistulising Crohn's disease. Gut. 2011;60(6):788-98.
43. Garcia-Olmo D, Herreros D, Pascual I, Pascual JA, Del-Valle E, Zorrilla J, et al. Expanded adipose-derived stem cells for the treatment of complex perianal fistula: a phase II clinical trial. Dis Colon Rectum. 2009;52(1):79-86.
44. Herreros MD, Garcia-Arranz M, Guadalajara H, De-La-Quintana P, Garcia-Olmo D, FATT Collaborative Group. Autologous expanded adipose-derived stem cells for the treatment of complex cryptoglandular perianal fistulas: a phase III randomized clinical trial (FATT 1: fistula Advanced Therapy Trial 1) and long-term evaluation. Dis Colon Rectum. 2012;55(7):762-72.
45. Ohki T, Yamato M, Murakami D, Takagi R, Yang J, Namiki H, et al. Treatment of oesophageal ulcerations using endoscopic transplantation of tissue-engineered autologous oral mucosal epithelial cell sheets in a canine model. Gut. 2006;55(12):1704-10.
46. Lee D-E, Koo H, Sun I-C, Ryu JH, Kim K, Kwon IC. Multifunctional nanoparticles for multimodal imaging and theragnosis. Chem Soc Rev. 2012;41(7):2656-72.
47. Wallace PK, Tario JD, Fisher JL, Wallace SS, Ernstoff MS, Muirhead KA. Tracking antigen-driven responses by flow cytometry: monitoring proliferation by dye dilution. Cytom Part J Int Soc Anal Cytol. 2008;73(11):1019-34.
48. Tassa C, Shaw SY, Weissleder R. Dextran-coated iron oxide nanoparticles: a versatile platform for targeted molecular imaging, molecular diagnostics, and therapy. Acc Chem Res. 2011;44(10):842-52.
49. Luciani N, Wilhelm C, Gazeau F. The role of cell-released microvesicles in the intercellular transfer of magnetic nanoparticles in the monocyte/macrophage system. Biomaterials. 2010;31(27):7061-9.
50. Silva AKA, Wilhelm C, Kolosnjaj-Tabi J, Luciani N, Gazeau F. Cellular transfer of magnetic nanoparticles via cell microvesicles: impact on cell tracking by magnetic resonance imaging. Pharm Res. 2012;29(5):1392-403.